Dielectric function and plasmonic behavior of Ga(II) and Ga(III)

YAEL GUTIÉRREZ,[1,2] MARIA LOSURDO,[2] PABLO GARCÍA-FERNÁNDEZ,[3] MARTA SAINZ DE LA MAZA,[1] FRANCISCO GONZÁLEZ,[1] APRIL S. BROWN,[4] HENRY O. EVERITT,[5,6] JAVIER JUNQUERA,[3] AND FERNANDO MORENO[1,2,*]

[1] *Optics Group, Department of Applied Physics, Faculty of Sciences, University of Cantabria, Avda. Los Castros s/n, Santander 39005, Spain*
[2] *Institute of Nanotechnology, CNR-NANOTEC, via Orabona 4, Bari 70126, Italy*
[3] *Departamento de Ciencias de la Tierra y Física de la Materia Condensada, Universidad de Cantabria, Cantabria Campus Internacional, Santander 39005, Spain*
[4] *Department of Electrical and Computer Engineering, Duke University, Durham, NC 27708, USA*
[5] *Department of Physics, Duke University, Durham, NC 27708, USA*
[6] *U.S. Army CCDC-Aviation & Missile Center, Redstone Arsenal, Alabama 35898, USA*
[*] *morenof@unican.es*

Abstract: In order to exploit gallium's (Ga) rich polymorphism in the design of phase-change plasmonic systems, accurate understanding of the dielectric function of the different Ga-phases is crucial. The dielectric dispersion profiles of those phases appearing at atmospheric pressure have been reported in the literature, but there is no information on the dielectric function of the high-pressure Ga-phases. Through first principles calculations we present a comprehensive analysis of the interdependence of the crystal structure, band structure, and dielectric function of two high-pressure Ga phases (Ga(II) and Ga(III)). The plasmonic behavior of these high-pressure Ga-phases is compared to those stable (liquid- and α-Ga) and metastable (β-, γ- and δ-Ga) at atmospherics pressure. This analysis can have important implications in the design of pressure-driven phase-change Ga plasmonic devices and high-pressure SERS substrates.

1. Introduction

Metallic gallium (Ga) undergoes a solid-liquid phase transition near room temperature, and recent research into its wide polymorphism (see Fig. 1) has identified a variety of applications for controlled Ga phase changes. Depending on temperature, Ga can exist in six different phases at atmospheric pressure (Fig. 1a), i.e., above 302.7 K Ga is a liquid metal (*l*-Ga, stable phase), and just below that temperature α-Ga is the solid thermodynamically stable phase [1], although at lower temperatures there are the additional Ga-phases: β-Ga with a melting temperature of $T_m = 256.8$ K [2], γ-Ga ($T_m = 237.6$ K) [3], ϵ-Ga ($T_m = 244.6$ K) [4], and δ-Ga ($T_m = 253.8$ K) [5]. This polymorphism characteristic of Ga, along with its recently demonstrated plasmonic response from the near-infrared to the UV [6,7] and its low tendency to oxidize [8], has been exploited for phase-change memories [9], reversible light-induced switching [10], phase-change systems for non-linear optics as described by Zheludev et al. in Ref. [11], and for emerging "active plasmonics" [12,13]. Most of these applications take advantage of the reflectivity change produced by the phase transition between Ga-phases induced either by optical [14] /e-beam [15] excitation or by heating [16]. The design of these types of devices has been severely hampered by the absence of trustworthy optical properties for each stable and metastable Ga-phase at atmospheric pressure.

A recent study has revealed that there are significant differences in the dielectric function of each phase, especially in the spectral region below 2.5 eV. Whereas α- and β-Ga present interband
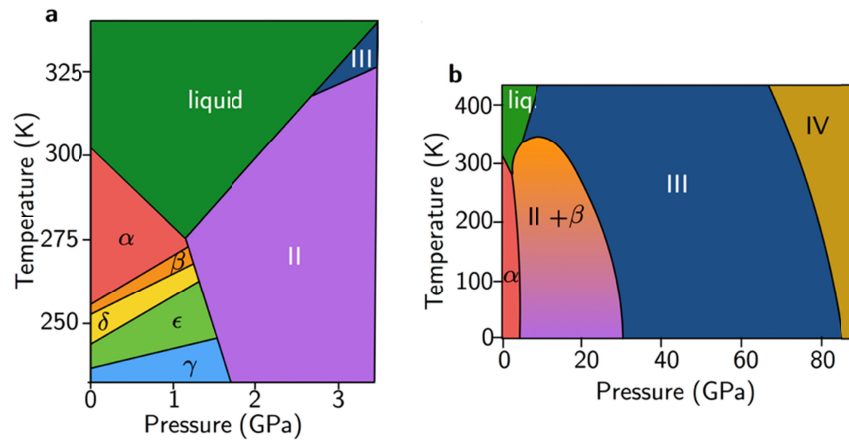
Fig. 1. (a) Phase diagram of bulk Ga adapted from Ref. [1], and (b) extended pressure-temperature phase diagram adapted from Ref. [17].

transitions below that energy, l- [18], γ-, and δ-Ga have Drude-like metallic behavior [19] at atmospheric pressure. Indeed, pressure is another parameter that may be exploited in active and phase-change plasmonics. Although several high-pressure stable Ga-phases have been reported in the literature (see Fig. 1) [1,17], i.e., Ga(II) (which according to Ref. [17] may coexists with β-Ga), Ga(III), Ga(IV), and Ga(V) [17,20–22], none of these previous studies have presented the optical properties of these high-pressure Ga-phases. Furthermore, the relationship between pressure and phase becomes very relevant for nanoparticles, where, because of the curvature radius, R, the Laplace pressure ($\Delta P = 2\gamma_{lv}/R$, being γ_{lv} the liquid/vapor surface tension) inside the nanoparticle can reach very high values (of the order of GPa) and induce high pressure phases [18].

Here, we report a comprehensive theoretical investigation of the optical response of both Ga(II) and Ga(III) - including their correlation with the respective crystalline structures and band diagrams - using dielectric functions calculated by first principles methods. Moreover, we evaluate the plasmonic response of Ga(II) and Ga(III), then compare it with the plasmonic response of the phase expected at atmospheric pressure, to evaluate the plasmon sensitivity to pressure changes. The conclusions of this research can open the way for the design of pressure driven phase-change Ga plasmonic devices and new plasmonic substrates for high-pressure surface-enhanced Raman spectroscopy (SERS) [23–25].

2. Methods

2.1. Computational details

Density functional first-principles calculations based on a numerical atomic orbital method were carried out using the SIESTA code [26]. All the calculations have been performed with the Generalized Gradient Approximation (GGA), using the exchange-correlation potential parametrized by Perdew-Burke-Ernzerhof (PBEsol) method [27], to simulate electronic exchange and correlations. Core electrons are described by ab-initio optimized norm-conserving pseudopotentials, generated following the recipe given by Hamann [28], and available in the PSEUDODOJO code [29,30] using the Kleinman-Bylander fully non-local separable representation. The $3s$, $3p$, $3d$, $4s$, and $4p$ electrons were considered as valence electrons of Ga and explicitly included in the calculations.

The one-electron Kohn Sham eigenvectors were expanded in a basis of localized numerical atomic orbitals (NAO), as implemented in the SIESTA code. The size of the basis set chosen was single ζ for the semicore $3s$ and $3p$ orbitals, double ζ for the $3d$ and $4p$ orbitals, and triple ζ for

the 4s orbitals. All parameters required to describe the shape and the range of the NAO were variationally optimized following the recipe in Refs. [31,32]. The optimal basis set is available upon request.

The electron density, Hartree, and exchange correlation potentials, as well as the corresponding matrix elements between the basis orbitals, were calculated in a uniform real space grid. The equivalent plane wave cut-off used to represent the charge density was 800 Ry. For the Brillouin integrations, we use a Monkhorst-Pack [33] sampling of $10 \times 10 \times 10$. For the structural characterization, atoms and unit cells were allowed to relax until the maximum component of the force acting on any atoms were smaller than 0.01 eV/Å, and the maximum component of the stress tensor was smaller than 0.0001 eV/Å^3.

2.2. Optical response

The interband contribution to the frequency-dependent dielectric function $\varepsilon(\omega) = \varepsilon_1(\omega) + i\varepsilon_2(\omega)$ of the studied structures was obtained using first-order time-dependent perturbation theory to calculate the dipolar transition matrix elements between occupied and unoccupied single-electron eigenstates as implemented in the SIESTA code. The frequency-dependent dielectric function can be written as

$$\varepsilon_2(\omega) = \frac{2\pi}{mN} \frac{\omega_p^2}{\omega^2} \sum_{v,c} \int_{BZ} \frac{d\mathbf{k}}{(2\pi)^3} |M_{cv\mathbf{k}}|^2 \delta(E_{c\mathbf{k}} - E_{v\mathbf{k}} - \hbar\omega) \tag{1}$$

where m is the electron mass, N is the number of electrons per unit volume, $\omega_p = (4\pi Ne^2/m)^{1/2}$ is the plasma frequency, and e is the electron charge. The single particle electronic states $|\psi\rangle$, of energy E are labeled by their crystal momentum $\mathbf{k}$ and their valence (v) and conduction (c) band index. The sum is over connecting valence and conduction states and over all $\mathbf{k}$ points in the first Brillouin zone. The optical matrix element is given by $M_{cv\mathbf{k}} = \langle \psi_{c\mathbf{k}} | \hat{\mathbf{e}} \cdot \mathbf{p} | \psi_{v\mathbf{k}} \rangle$ in the dipolar approximation, where $\hat{\mathbf{e}}$ is the polarization of the incident light and $\mathbf{p}$ is the momentum operator. The real part of the dielectric function $\varepsilon_1(\omega)$ can be obtained from the imaginary part using the Kramers-Kronig relation. In this approach excitonic and intraband contributions are not considered.

For analyzing the origin of the peaks appearing in the $\varepsilon_2(\omega)$ spectra due to interband transitions, we have calculated the values of the optical matrix element $M_{cv\mathbf{k}}$ for every pair of conduction and valence bands at each $\mathbf{k}$ point with an energy difference equal to the photon energy at which the peak appears. In this way, we can analyze the pair of bands contributing to the interband transition visible in $\varepsilon_2(\omega)$ spectra. All bands have been included in the optical calculations of each Ga phase. The optical mesh is $40 \times 40 \times 40$, and the Gaussian broadening has been set to 0.20 eV.

2.3. Reflectance and electromagnetic calculations

Reflectance calculations have been performed using the Transfer Matrix Method (TMM), which also allows the calculation of the transmittance and absorbance spectra of an arbitrary system of homogeneous, non-magnetic multilayers. We have considered Ga films of thickness $h = 150$ nm deposited on an infinite sapphire substrate (refractive index $n = 1.78$) and exposed to air. This value of h is consistent with experimental values typically found in the literature [13, 16]. The angle between the wave-vector $\mathbf{k}$ and the surface's normal (AOI) has been fixed to $0°$ (normal incidence). The absorption cross-section and near-field enhancement in Ga hemispheres on substrates have been calculated using the COMSOL Multiphysics package (COMSOL Inc., Burlington, MA, USA). The refractive index of the substrate (sapphire, Al$_2$O$_3$) has been taken from Ref. [34].

3.   Results

3.1.   Crystal and electronic structures

Figures 2(a,d) illustrate the unit cell for the Ga(II) and Ga(III) phases. Ga(II) crystallizes in a body-centered cubic structure with space group symmetry *I-43d* (no 220) and a unit cell that contains 12 atoms. Ga(III) crystallizes in a body-centered tetragonal cell with space group symmetry *I4/mmm* (no 139) and two atoms in its unit cell.
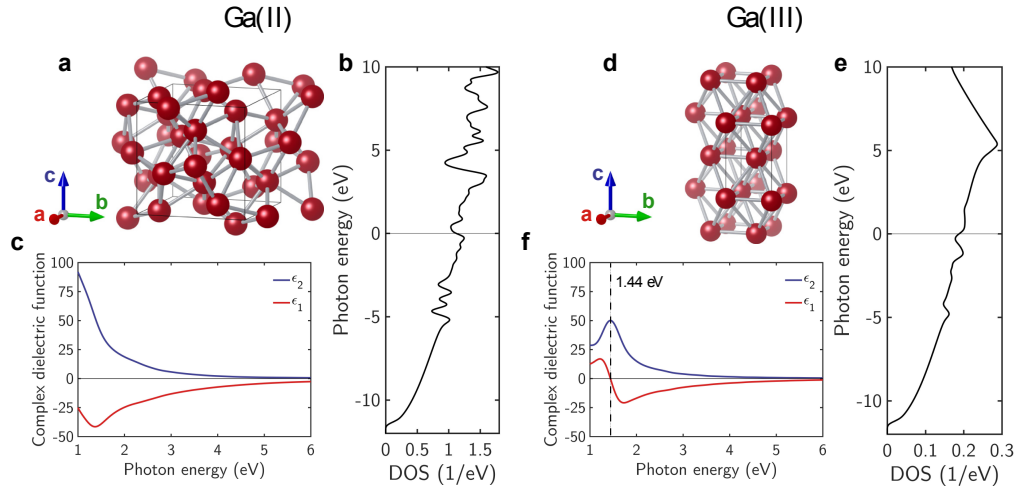

Fig. 2. (a,d) Structure of the unit cell, (b,e) density of states DOS, and (c,f) complex dielectric function ($\varepsilon = \varepsilon_1 + i\varepsilon_2$) of Ga(II) (left) and Ga(III) (right).

Using density functional theory (DFT) calculations as implemented in SIESTA (see Methods) we calculated the theoretical lattice parameters and atomic positions (see Table 1). Their reliability can be assessed by the favorable comparison with the experimentally obtained values also reported in the table. The density of states (DOS) for both phases exhibits metallic behavior, although we shall see that the dip appearing around the Fermi energy is clearly reflected in the optical properties.

Table 1. Theoretical lattice constants, structural parameters, and atomic coordinates of Ga(II) and Ga(III). Some experimental values are added for reference.

Ga II			Ga III		
Property	This work	Experiment [1]	Property	This work	Experiment [1]
Lattice Parameters			Lattice Parameters		
$|a|$(Å)	5.991	5.951 ± 0.005	$|a|$(Å)	2.967	2.813 ± 0.003
$|b|$(Å)	5.991	5.951 ± 0.005	$|b|$(Å)	2.967	2.813 ± 0.003
$|c|$(Å)	5.991	5.951 ± 0.005	$|c|$(Å)	4.109	4.452 ± 0.005
θ_{bc} (°)	90.00	90.00	θ_{bc} (°)	90.00	90.00
θ_{ac} (°)	90.00	90.00	θ_{ac} (°)	90.00	90.00
θ_{ab} (°)	90.00	90.00	θ_{ab} (°)	90.00	90.00
Coordinates (Å)			Coordinates (Å)		
x_{GaI}	2.247	2.096	x_{GaI}	0.000	0.000
y_{GaI}	0.000	0.000	y_{GaI}	0.000	0.000
z_{GaI}	1.498	1.398	z_{GaI}	0.000	0.000

The computed complex dielectric function for each phase are shown in Figs. 2(c,f). On the one hand, Ga(II) presents metallic behavior ($\varepsilon_1 < 0$) in all the studied spectral range. However, the dip in the DOS around the Fermi energy is reflected in the increasing value of ε_1 below 1.5 eV. On the other hand, Ga(III) presents interband transitions at 1.44 eV. These interband transitions are indicated with arrows in Fig. 3 and have been identified by evaluating the values of the optical matrix element $M_{cv\mathbf{k}}$ for every pair of conduction (c) and valence bands (v) at each **k** point along the high symmetry lines in the first Brillouin zone (see Methods). The strength of the color of the arrows indicates the intensity of the transition based on the evaluation of $M_{cv\mathbf{k}}$.
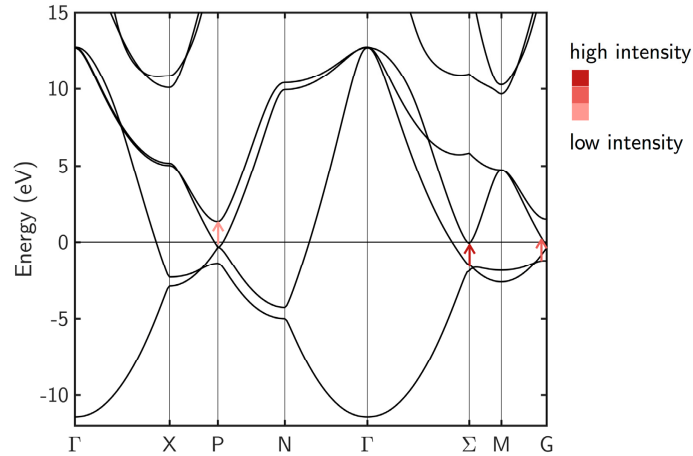

Fig. 3. Band diagram of Ga(III). Arrows indicate the interband transitions manifested in its complex dielectric function at 1.44 eV. The strength of the color of the arrows indicates the intensity of the transition, based on the evaluation of $M_{cv\mathbf{k}}$.

The extended pressure-temperature phase diagram reported by Schule and Holzapfel in Ref. [17] shows that Ga(II) may coexists with β-Ga (see Fig. 1(b)). Therefore, the optical response of Ga in that region should be modelled with an effective complex dielectric function built as mixture of the dielectric functions of Ga(II) and β-Ga. Among the different effective medium approximations, Bruggeman (BEMA) is the most suitable mixing methodology for modelling this system since it is constituted by a completely random inhomogeneous media whose components (Ga(II) and β-Ga) are treated symmetrically [35]. This procedure has been used to model the dielectric function of cooled liquid Ga samples whose XRD spectra have shown to be composed by a mixture of α-/β-Ga and α-/γ-Ga [19]. Figure 4 shows the effective dielectric function of a mixture of Ga(II) and β-Ga a calculated using BEMA with different Ga(II) filling fractions ($f_{Ga(II)}$). The dielectric functions of pure Ga(II) and β-Ga are plotted for reference.

3.2. Plasmonic behavior

The plasmonic performance of Ga(II) and Ga(III) phases has been compared with that of other Ga-phases by the evaluation of two metrics related to localized surface plasmons (LSP) in nanoparticles. Within the quasistatic approximation, the Fröhlich frequency (E_{Fr}) (i.e., the frequency at which ($\varepsilon_1 = -2$) corresponds to the energy at which localized surface plasmon resonances LSPRs are excited in isolated spherical metallic particles whose size is much smaller than the illuminating wavelength. The Faraday number (Fa), as proposed by Lalisse et al. in Ref. [36], is a dimensionless metric that quantifies the ability of a nanoparticle to enhance the electric field intensity in its surrounding medium. Thus, interesting plasmonic materials are characterized by high Fa numbers.
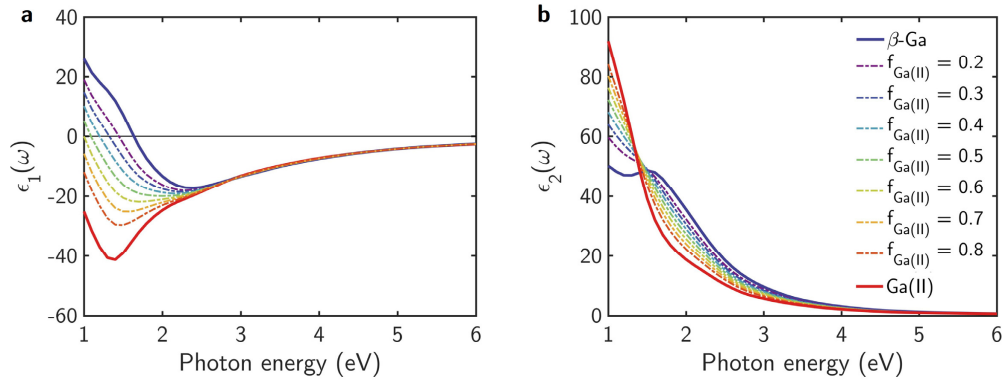
Fig. 4. (a) Real and (b) imaginary part of the effective dielectric function ($\varepsilon = \varepsilon_1 + i\varepsilon_2$) of a mixture of Ga(II) and β-Ga obtained using Bruggeman effective medium approximation with different Ga(II) filling fractions $f_{Ga(II)}$ (dashed lines). Red and blue solid lines represent the dielectric function of Ga(II) and β-Ga, respectively.

Figure 5 shows the values of the *Fa* number of each Ga-phase, including those phases stable at room pressure (i.e., α-, β-, γ-, δ- and *l*-Ga), versus their Fröhlich frequency. The Faraday number can also be related to the free-electron behavior of each phase: good plasmonic metals have low values of ε_2 and negative values of ε_1. Therefore, the lower the values of ε_2, the higher the corresponding *Fa* numbers. Keeping this in mind, the plasmonic performance of Ga(II) is superior to that of both α- and β-Ga. This behavior can be related to the optical properties of these materials: Ga(II) has metallic behavior in all the analyzed spectral range whereas α- and β-Ga present interband transitions below 2 eV. Conversely, the interband transitions in Ga(III) at 1.44 eV produce a plasmonic performance comparable to that of α-Ga. Therefore, if we correlate the values of *Fa* to the free-electron behavior of each phase, we can list the Ga-phases in increasing order of free-electron behavior as: Ga(III), α-Ga, β-Ga, Ga(II), γ-Ga, δ-Ga, and *l*-Ga. This is consistent with results reported in Ref. [19].
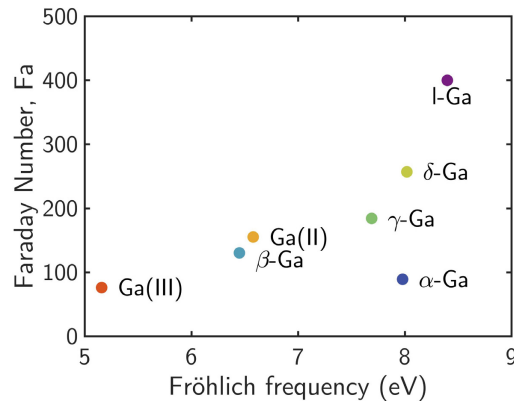

Fig. 5. Faraday number vs Fröhlich frequency of the different Ga-phases.

All Ga-phases present a Fröhlich energy in the UV range (photon energies above 3 eV), which makes Ga a promising candidate for UV plasmonics applications [37,38]. It is worth noting that common metals used for plasmonic in the visible range (i.e., Ag with $E_{Fr} = 3.5$ eV or Au $E_{Fr} = 2.7$ eV) present interband transitions below 3 eV that inhibit their use in UV plasmonics.

Although Ga-phases have lower Faraday numbers than other metals that have been proposed for UV plasmonics, such as Al ($Fa = 1391$ and $E_{Fr} = 8.9$ eV) or Mg ($Fa = 6542$ and $E_{Fr} = 5.7$ eV) [38], the oxide shell that forms on Ga NPs stabilizes to only ~1 nm thick. Conversely, in the case of Al or Mg, oxidation can consume all metal in nanoparticles made of these metals, inhibiting their plasmonic response [39,40]. Rh has been recently proposed as an alternative to Al and Mg in UV plasmonics applications due to its stability against various environments [41,42]. However, its plasmonic performance is lower than that of the different Ga-phases ($Fa = 59$ and $E_{Fr} = 8.1$ eV) [38].

Indeed, the near-field enhancement produced by hemispherical l-Ga NPs has already been exploited in surface-enhanced Raman spectroscopy (SERS) experiments [43,44]. Due to the increasing interest in performing SERS experiments at high pressure [23–25] -already SERS experiments up to 10 GPa have been performed [24]-, Ga(II) and Ga(III) NPs seem promising candidates as substrates for high-pressure SERS. The reported values of their optical constants can help the rational design of Ga(II) and Ga(III) nanostructures for this purpose. In order to explore this possibility, we have calculated the absorption cross-section, C_{abs}, and the average near-field enhancement, $\langle|\mathbf{E}|^2\rangle$, over the surface of hemispherical NPs with radius $R = 60$ nm, made of Ga(II) and Ga(III), respectively, and located on a sapphire substrate (see Figs. 6(a,b) red lines).
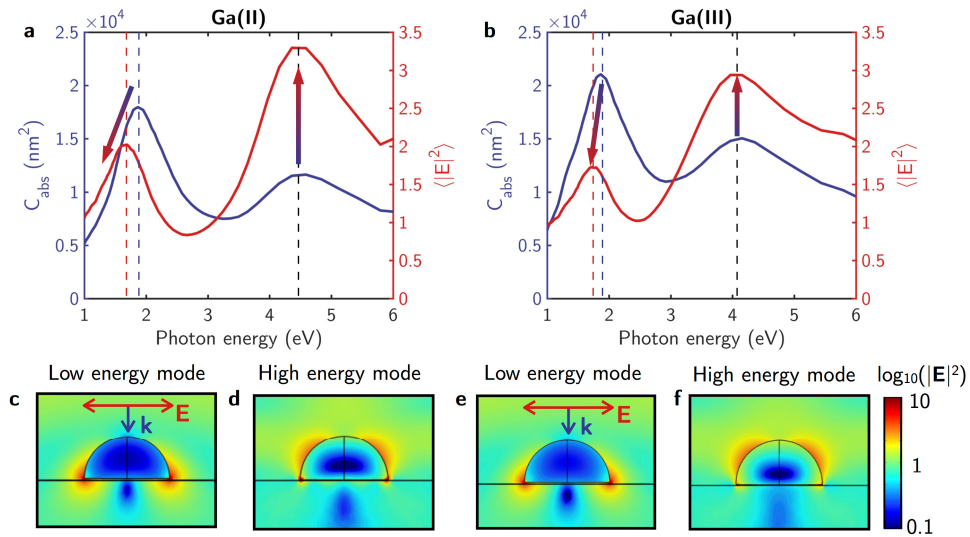

Fig. 6. Absorption cross-section (Cabs, blue line) and near-field enhancement averaged $\langle|\mathbf{E}|^2\rangle$ red line) over the surface of (a) Ga(II) and (b) Ga(III) $R = 60$ nm hemispherical NPs on an infinite sapphire substrate embedded in air. Respective near-field distributions $(\log_{10}(|\mathbf{E}|^2))$ of their (c, e) low and (d, f) high energy modes. Red and blue arrows indicate the electric field (**E**) and wave vectors (**k**), respectively.

As reported for the other Ga-phases [19], the hemispherical NPs present two modes: a low energy mode of dipolar character, where the near-field is highly localized in the interface between the NPs and the substrate (see Figs. 6(c,e)), and a high energy mode of higher order, where the field is more evenly distributed over the hemisphere's surface (see Figs. 6(d,f)). In the former case, although the *hot-spots* are more intense, the average near field enhancement over the NPs surface $\langle|\mathbf{E}|^2\rangle$ is lower because the *hot-spots* are localized in a smaller region (i.e., the around sharp edge in the NPs-substrate interface). Conversely, in the latter, although the hots-spots are less intense, since they are more evenly distributed on the NPs surface $\langle|\mathbf{E}|^2\rangle$ takes higher values.

In light of the near-field distribution, the excitation of the high energy mode seems to be more convenient for SERS experiments: due to the even distribution of the near-field, the deposition of the molecules is not as a critical factor as in the low energy mode for which the molecules have to be precisely deposited in the NP-substrate interface. In addition, the evaluation of the near-field enhancement $\langle |\mathbf{E}|^2 \rangle$ over the NPs surface indicates that for the high energy mode, its magnitude is ~1.5 times higher than for the low energy one. Specifically, Ga(II) hemispheres produce higher near field enhancement than those made of Ga(III) at both modes (in agreement with Fig. 5), although the values of their absorption cross-sections C_{abs} are lower.

By comparing C_{abs} and $\langle |\mathbf{E}|^2 \rangle$ in Figs. 6(a,b), we discover that the spectral positions of their corresponding high energy peaks are the same. This feature presents an additional advantage when designing SERS substrates from hemispherical NPs: a far-field measurement (C_{abs}) indicates the exact photon energy that produces the maximum near-field enhancement. Conversely, the low energy peak in the C_{abs} spectrum is red-shifted with respect to that of the $\langle |\mathbf{E}|^2 \rangle$ spectrum. This red-shift phenomenon has already been reported for dipolar nano-antennas [45] and is smaller for the Ga(III) hemispheres than for Ga(II) (0.1 vs 0.2 eV, respectively).

Many of the reported Ga-based phase change devices reported in the literature rely in the change of reflectivity produced by the phase transition between Ga-phases induced either by optical [14] or *e*-beam [15] excitation or by heating [16]. In order to explore the change in reflectivity by a transition between Ga-phases induced by an applied pressure, Fig. 7(a) plots the reflectance spectrum at normal incidence of a layer 150 nm thick, made of the different Ga-phases on a sapphire substrate (see Methods). As expected, the largest differences in the reflectance spectra of the different Ga-phases is produced below ≈ 2 eV. Those phases with interband transitions below ≈ 2 eV (i.e., α-, β-Ga and Ga (III)) show lower reflectance values because of their dielectric behavior ($\varepsilon_1 > 0$) [19]. Above 2 eV, their reflectance increases because at those energies their dielectric function become metallic ($\varepsilon_1 < 0$). By contrast, those phases with a metallic dielectric function in all the analyzed spectral range (i.e., γ-Ga, δ-Ga, *l*-Ga and Ga(II)) present almost constant reflectance. For the sake of comparison, in Table 2 the values of reflectance of each Ga-phase at 1 and 6 eV are summarized. Whilst α-, β-Ga and Ga (III), the change in reflectance from 1 to 6 eV is ~20%, for γ-Ga, δ-Ga, *l*-Ga, and Ga(II) the change is ~5%.
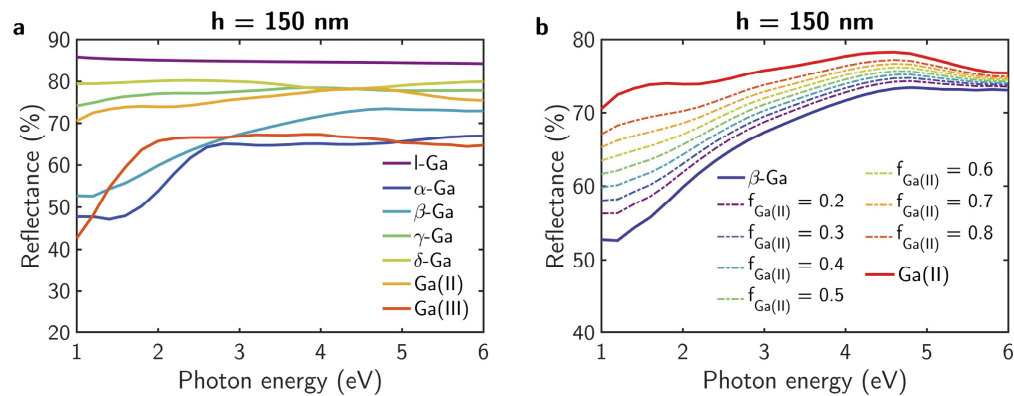

Fig. 7. (a) Reflectance spectra at normal incidence of a layer 150 nm thick made of the different Ga-phases on a sapphire substrate. (b) Reflectance spectrum at normal incidence of a layer $h = 150$ nm thick made of a mixture of β-Ga and Ga(II) on a sapphire substrate with different Ga(II) filling fractions $f_{Ga(II)}$.

Since the extended pressure-temperature phase diagram reported by Schule and Holzapfel in Ref. [17] shows that Ga(II) coexists with β-Ga, Fig. 7(b) shows the reflectance of a layer 150

Table 2. Reflectance (%) at normal incidence of a layer $h = 150$ nm thick made of the different Ga-phases on a sapphire substrate at 1 and 6 eV.

Photon energy	l-Ga	α-Ga	β-Ga	γ-Ga	δ-Ga	Ga(II)	Ga(III)
1 eV	85.9	47.7	52.7	74.1	79.5	70.5	42.6
6 eV	84.3	66.9	72.9	77.8	79.9	75.4	64.6

nm thick made of a mixture of β-Ga and Ga(II) on a sapphire substrate with different Ga(II) filling fractions $f_{Ga(II)}$. As before, the optical constants of each mixture have been obtained using BEMA (see Fig. 4).

4. Conclusions

In conclusion, we have reported the first detailed analysis of the optical properties of Ga(II) and Ga(III), two of the high-pressure Ga phases, and their correlation with their crystalline and electronic structures. It was found that whereas Ga(II) has metallic dielectric function in the 1-6 eV spectral range, Ga(III) presented interband transitions at 1.44 eV. We have compared the plasmonic performance of these two high pressure phases with those stable and metastable phases at atmospheric pressure. Ga(III) has a plasmonic performance comparable to that of α-Ga, the phase most common at atmospheric pressure and room temperature, while Ga(II) has a plasmonic performance superior to that of α- and β-Ga. Inspired by the recent use of liquid-Ga hemispheres as SERS substrates [43,44], we analyzed the near-field enhancement produced by Ga(II) and Ga(III) hemispheres on a sapphire substrate to evaluate their applicability to high pressure SERS. Ga(II) hemispherical particles produce near-field enhancements ~1.5 times more intense than Ga(III) hemispheres. In addition, because many phase-change devices rely in the change of reflectivity produced by the transition between Ga-phases, we have compared the reflectance spectra of a thin film made of the different Ga polymorphs. It can be concluded that the largest differences are produced below 2 eV, where some of the Ga-phases have interband transitions. This work confirms the potential for pressure driven phase-change Ga plasmonic devices and plasmonic substrates for high-pressure SERS [23–25].

References

1. L. Bosio, "Crystal structures of Ga(II) and Ga(III)," J. Chem. Phys. **68**(3), 1221–1223 (1978).
2. L. Bosio, A. Defrain, H. Curien, and A. Rimsky, "Structure cristalline du gallium β," Acta Crystallogr., Sect. B: Struct. Crystallogr. Cryst. Chem. **25**(5), 995 (1969).

3. L. Bosio, H. Curien, M. Dupont, and A. Rimsky, "Structure cristalline de Gaγ," Acta Crystallogr., Sect. B: Struct. Crystallogr. Cryst. Chem. **28**(6), 1974–1975 (1972).
4. L. Bosio, R. Cortes, J. R. D. Copley, W. D. Teuchert, and J. Lefebvre, "Phonons in metastable beta gallium: neutron scattering measurements," J. Phys. F: Met. Phys. **11**(11), 2261–2273 (1981).
5. L. Bosio, H. Curien, M. Dupont, and A. Rimsky, "Structure cristalline de Gaδ," Acta Crystallogr., Sect. B: Struct. Crystallogr. Cryst. Chem. **29**(2), 367–368 (1973).
6. P. C. Wu, T.-H. Kim, A. S. Brown, M. Losurdo, G. Bruno, and H. O. Everitt, "Real-time plasmon resonance tuning of liquid Ga nanoparticles by in situ spectroscopic ellipsometry," Appl. Phys. Lett. **90**(10), 103119 (2007).
7. P. C. Wu, M. Losurdo, T.-H. Kim, S. Choi, G. Bruno, and A. S. Brown, "In situ spectroscopic ellipsometry to monitor surface plasmon resonant group-III metals deposited by molecular beam epitaxy," J. Vac. Sci. Technol., B: Microelectron. Nanometer Struct.–Process., Meas., Phenom. **25**(3), 1019 (2007).
8. Y. Gutierrez, D. Ortiz, J. M. Sanz, J. M. Saiz, F. Gonzalez, H. O. Everitt, and F. Moreno, "How an oxide shell affects the ultraviolet plasmonic behavior of Ga, Mg, and Al nanostructures," Opt. Express **24**(18), 20621 (2016).
9. B. F. Soares, F. Jonsson, and N. I. Zheludev, "All-optical phase-change memory in a single gallium nanoparticle," Phys. Rev. Lett. **98**(15), 153905 (2007).
10. N. I. Zheludev, "Single nanoparticle as photonic switch and optical memory element," J. Opt. A: Pure Appl. Opt. **8**(4), S1–S8 (2006).
11. A. V. Krasavin, K. F. MacDonald, A. S. Schwanecke, and N. I. Zheludev, "Gallium/aluminum nanocomposite material for nonlinear optics and nonlinear plasmonics," Appl. Phys. Lett. **89**(3), 031118 (2006).
12. A. V. Krasavin and N. I. Zheludev, "Active plasmonics: controlling signals in Au/Ga waveguide using nanoscale structural transformations," Appl. Phys. Lett. **84**(8), 1416–1418 (2004).
13. A. V. Krasavin, A. V. Zayats, and N. I. Zheludev, "Active control of surface plasmon–polariton waves," J. Opt. A: Pure Appl. Opt. **7**(2), S85–S89 (2005).
14. K. F. MacDonald, V. A. Fedotov, S. Pochon, G. Stevens, F. V. Kusmartsev, V. I. Emel'yanov, and N. I. Zheludev, "Controlling the coexistence of structural phases and the optical properties of gallium nanoparticles with optical excitation," Europhys. Lett. **67**(4), 614–619 (2004).
15. S. Pochon, K. F. MacDonald, R. J. Knize, and N. I. Zheludev, "Phase coexistence in gallium nanoparticles controlled by electron excitation," Phys. Rev. Lett. **92**(14), 145702 (2004).
16. S. R. C. Vivekchand, C. J. Engel, S. M. Lubin, M. G. Blaber, W. Zhou, J. Y. Suh, G. C. Schatz, and T. W. Odom, "Liquid plasmonics manipulating surface plasmon polaritons via phase transitions," Nano Lett. **12**(8), 4324–4328 (2012).
17. O. Schulte and W. B. Holzapfel, "Effect of pressure on the atomic volume of Ga and Tl up to 68 GPa," Phys. Rev. B **55**(13), 8122–8128 (1997).
18. M. Losurdo, A. Suvorova, S. Rubanov, K. Hingerl, and A. S. Brown, "Thermally stable coexistence of liquid and solid phases in gallium nanoparticles," Nat. Mater. **15**(9), 995–1002 (2016).
19. Y. Gutiérrez, M. Losurdo, P. García-Fernández, M. Sainz de la Maza, F. González, A. S. Brown, H. O. Everitt, J. Junquera, and F. Moreno, "Gallium polymorphs: phase-dependent plasmonics," Adv. Opt. Mater. **1900307**, 1900307 (2019).
20. T. Kenichi, K. Kazuaki, and A. Masao, "High-pressure bct-fcc phase transition in Ga," Phys. Rev. B **58**(5), 2482–2486 (1998).
21. Z. Li and J. S. Tse, "High-pressure bct to fcc structural transformation in Ga," Phys. Rev. B **62**(15), 9900–9902 (2000).
22. L. Comez, A. Di Cicco, J. Itié, and A. Polian, "High-pressure and high-temperature x-ray absorption study of liquid and solid gallium," Phys. Rev. B **65**(1), 014114 (2001).
23. P. Wang, H. Li, J. Jiang, B. Mo, and C. Cui, "An exploration of surface enhanced Raman spectroscopy (SERS) for in situ detection of sulfite under high pressure," Vib. Spectrosc. **100**(99), 172–176 (2019).
24. Y. Fu and D. D. Dlott, "Single molecules under high pressure," J. Phys. Chem. C **119**(11), 6373–6381 (2015).
25. P. Podini and J. M. Schnur, "Applicability of sers to the study of adsorption at high pressure," Chem. Phys. Lett. **93**(1), 86–90 (1982).
26. J. M. Soler, E. Artacho, J. D. Gale, A. García, J. Junquera, P. Ordejón, and D. Sánchez-Portal, "The SIESTA method for ab initio order- N materials simulation," J. Phys.: Condens. Matter **14**(11), 2745–2779 (2002).
27. J. P. Perdew, A. Ruzsinszky, G. I. Csonka, O. A. Vydrov, G. E. Scuseria, L. A. Constantin, X. Zhou, and K. Burke, "Restoring the density-gradient expansion for exchange in solids and surfaces," Phys. Rev. Lett. **100**(13), 136406 (2008).
28. D. R. Hamann, "Optimized norm-conserving Vanderbilt pseudopotentials," Phys. Rev. B **88**(8), 085117 (2013).
29. A. García, M. J. Verstraete, Y. Pouillon, and J. Junquera, "The psml format and library for norm-conserving pseudopotential data curation and interoperability," Comput. Phys. Commun. **227**, 51–71 (2018).
30. M. J. van Setten, M. Giantomassi, E. Bousquet, M. J. Verstraete, D. R. Hamann, X. Gonze, and G.-M. Rignanese, "The PseudoDojo: Training and grading a 85 element optimized norm-conserving pseudopotential table," Comput. Phys. Commun. **226**(3), 39–54 (2018).
31. J. Junquera, Ó Paz, D. Sánchez-Portal, and E. Artacho, "Numerical atomic orbitals for linear-scaling calculations," Phys. Rev. B **64**(23), 235111 (2001).

32. E. Anglada, J. M. Soler, J. Junquera, and E. Artacho, "Systematic generation of finite-range atomic basis sets for linear-scaling calculations," Phys. Rev. B **66**(20), 205101 (2002).

33. H. J. Monkhorst and J. D. Pack, "Special points for Brillouin-zone integrations," Phys. Rev. B **13**(12), 5188–5192 (1976).

34. A. K. Harman, S. Ninomiya, and S. Adachi, "Optical constants of sapphire (α-Al$_2$O$_3$) single crystals," J. Appl. Phys. **76**(12), 8032–8036 (1994).

35. D. A. G. Bruggeman, "Berechnung verschiedener physikalischer Konstanten von heterogenen Substanzen. I. Dielektrizitätskonstanten und Leitfähigkeiten der Mischkörper aus isotropen Substanzen," Ann. Phys. **416**(7), 636–664 (1935).

36. A. Lalisse, G. Tessier, J. Plain, and G. Baffou, "Quantifying the efficiency of plasmonic materials for near-field enhancement and photothermal conversion," J. Phys. Chem. C **119**(45), 25518–25528 (2015).

37. J. M. Sanz, D. Ortiz, R. Alcaraz de la Osa, J. M. Saiz, F. González, A. S. Brown, M. Losurdo, H. O. Everitt, and F. Moreno, "UV Plasmonic behavior of various metal nanoparticles in the near- and far-field regimes: geometry and substrate effects," J. Phys. Chem. C **117**(38), 19606–19615 (2013).

38. Y. Gutiérrez, R. Alcaraz, D. Osa, D. Ortiz, J. M. Saiz, F. González, and F. Moreno, "Plasmonics in the ultraviolet with aluminum, gallium, magnesium and rhodium," Appl. Sci. **8**(1), 64 (2018).

39. M. W. Knight, N. S. King, L. Liu, H. O. Everitt, P. Nordlander, and N. J. Halas, "Aluminum for plasmonics," ACS Nano **8**(1), 834–840 (2014).

40. Y. Gutiérrez, M. M. Giangregorio, F. Palumbo, A. S. Brown, F. Moreno, and M. Losurdo, "Optically addressing interaction of Mg / MgO plasmonic systems with hydrogen," Opt. Express **27**(4), A197–A205 (2019).

41. A. M. Watson, X. Zhang, R. Alcaraz de la Osa, J. Marcos Sanz, F. González, F. Moreno, G. Finkelstein, J. Liu, and H. O. Everitt, "Rhodium nanoparticles for ultraviolet plasmonics," Nano Lett. **15**(2), 1095–1100 (2015).

42. X. Zhang, P. Li, Á Barreda, Y. Gutiérrez, F. González, F. Moreno, H. O. Everitt, and J. Liu, "Size-tunable rhodium nanostructures for wavelength-tunable ultraviolet plasmonics," Nanoscale Horiz. **1**(1), 75–80 (2016).

43. P. C. Wu, C. G. Khoury, T.-H. Kim, Y. Yang, M. Losurdo, G. V. Bianco, T. Vo-Dinh, A. S. Brown, and H. O. Everitt, "Demonstration of surface-enhanced Raman scattering by tunable, plasmonic gallium nanoparticles," J. Am. Chem. Soc. **131**(34), 12032–12033 (2009).

44. Y. Yang, J. M. Callahan, T. H. Kim, A. S. Brown, and H. O. Everitt, "Ultraviolet nanoplasmonics: A demonstration of surface-enhanced raman spectroscopy, fluorescence, and photodegradation using gallium nanoparticles," Nano Lett. **13**(6), 2837–2841 (2013).

45. F. Moreno, P. Albella, and M. Nieto-Vesperinas, "Analysis of the spectral behavior of localized plasmon resonances in the near- and far-field regimes," Langmuir **29**(22), 6715–6721 (2013).